IOP Publishing
Measurement Science and Technology
Meas. Sci. Technol. **31** (2020) 047001 (7pp)
https://doi.org/10.1088/1361-6501/ab46ff

Technical Note

A low-cost liquid refractive index sensor based on plastic optical fibre and CCD array

Daniel P Duarte[1,2], **Rogério N Nogueira**[1] and **Lúcia B Bilro**[1]

[1] Instituto de Telecomunicações—Polo de Aveiro, Aveiro 3810-193, Portugal
[2] Department of Physics, Aveiro University, Aveiro 3810-193, Portugal

E-mail: dduarte@av.it.pt

Received 5 August 2019, revised 9 September 2019
Accepted for publication 23 September 2019
Published 9 January 2020

Abstract

A wireless refractive index sensor for in-line measurement in liquids was developed. It is based on the Fresnel reflection on a prism–liquid interface, where the critical angle of the totally reflected light in the interface of two media is detected by a charge-coupled device (CCD) array. A LED is used as a light source and a plastic optical fibre, with a well-established numeric aperture, guides the light to the prism interface. Both the LED and the CCD are controlled with a Raspberry Pi 3 Model B board with wireless communication. Resolutions with values lower than 1.0×10^{-4} RIU can be achieved with this potential low-cost configuration.

Keywords: refractive index sensor, wireless, in-line measurement, liquids

(Some figures may appear in colour only in the online journal)

1. Introduction

In complex fluids, such as drinks, oil solutions, glycol solutions such as antifreeze, and inaccessible liquids such as the electrolyte of rechargeable cells, the refractive index (RI) can be measured for concentration assessment of dissolved or submicronic materials like sugar, alcohol and other substances [1]. RI is represented as a dimensionless number and described by a factor of which the speed of light with a certain wavelength propagates through the medium in comparison to their speed value in vacuum. Therefore, it is an important parameter in the characterization of a material. These different velocities in materials will possess refractive and reflective light effects between their interfaces, depending on the angle of light incidence.

Refractometers were developed and commercialized in 1881 by Ernst Abbe with a design that is still in use today, known as an Abbe refractometer. It uses two prisms between which a sample to be measured is placed. Light from a monochromatic source enters through one of the prisms until it reaches the sample, where refraction and total reflection will occur at a critical angle. The light will then exit the other prism to a scaled telescope that will search for the angle with a dark/illuminated boundary area, observed in a position that is dependent on the sample RI [2]. Resolutions in an order of magnitude of 10^{-4} RIU are commonly observed with this design. Laboratory digital refractometers are usually used as the preferred commercial application since they present higher resolution measurements, with precision in an order of magnitude of 10^{-4} to 10^{-5} RIU [3]. The phenomena of the total reflection of light between the interface of two mediums, typically a prism and a measured liquid, is the base principle of operation of this type of refractometer. The prism will serve as the sample holder while light comes from a long-life LED and is focused onto the prism surface boundary via a lens system. Depending on the RI of the liquid, the incoming light is partly transmitted into the sample if it is below the critical angle of total reflection, whereas for higher angles the light is totally reflected. These light reflections are RI dependent and detected by a high-resolution charge-coupled device (CCD) sensor array [1, 3]. These commercial RI sensors are mainly found in bench formats while in-line and real-time monitoring

solutions are comparatively rare and expensive, since they must be custom made.

Other RI sensors can also be found in academia. These include such optical fibre intrinsic sensing mechanisms as macrobending [4], D-shape [5], tapers [6], U-shaped clad removed tapers [7] and twisted tapers [8]. The use of fibre gratings, fibre Bragg gratings (FBGs), tilted FBGs (TFBGs) and long-period fibre gratings (LPFGs) have also been common subjects of development in interferometric-based sensors. Examples include etched FBG Fabry–Pérot sensors [9], LPFG Fabry–Pérot tapers [10], and TFBG [11]. Other type of interferometric RI sensors that do not use gratings but other fibre elements instead are those such as Fabry–Pérot photonic-crystal fibre (PCF) sensors [12], Sagnac loop PCFs [13], P–D fibre Sagnac loops [14], Michelson taper interferometers [15], core offset Mach–Zehnder [16], and microfluidic PCF sensors [17]. Surface plasmon resonance (SPR)-based sensors are also a very common research subject for RI sensors using both prism- [18] and fibre-based interrogation mechanisms. The latter includes uncladded fibre metal films [19], uncladded fibre metal nanoparticles [20], D-shaped fibre metal films [21] and tapers [22], as well as using tilted gratings to promote SPR interaction [23]. All the resolutions and RI ranges of these sensors are summarized in table 1. Although the interferometric and SPR sensors present high resolution and are potentially easy to apply in in-line and real-time monitoring systems, a spectral interrogation system is mandatory for data acquisition, which increases substantially the costs for a commercial application.

In this work the development of a low-cost RI sensor design is presented based on the following premises: (i) it can be implemented for in-line and real-time sensing with wireless capabilities; (ii) it offers low-cost development and implementation; (iii) it presents low complexity and high reproducibility; and (iv) it has the highest possible resolution per cost rate. With these criteria in consideration, a prism-based refractometer, adapted for in-line measurements, presents the best solution that meets all the stated requirements.

1.1. Sensor design

As mentioned before, the designed and developed RI sensor uses the light interaction between two different media, chiefly consisting of a prism and a measured solution. The working principle of this technology is based on the Fresnel reflection of unpolarised light, where reflection (R) is described by the Fresnel equations:

$$R = \frac{1}{2}\left(\left|\frac{n_1\cos(\theta_i) - n_2\cos(\theta_t)}{n_1\cos(\theta_i) + n_2\cos(\theta_t)}\right|^2 + \left|\frac{n_1\cos(\theta_t) - n_2\cos(\theta_i)}{n_1\cos(\theta_t) + n_2\cos(\theta_i)}\right|^2\right) \quad (1)$$

where n_1 and n_2 are the refractive indices of the first and second medium, respectively, and θ_i and θ_t are the angles of incident and transmitted light to and from the interface, respectively. The operation of this refractometer was designed to acquire the critical angle at which light is totally reflected between the interface of two media. A fused silica glass prism (triangular base of 30 × 30 × 30 mm) with a RI (n_1) of 1.46 was used as the component in contact with the liquid (n_2), and where light will propagate. In this component, it is important to guarantee that the material has a RI higher than the one expected from the liquid to be measured. The fulfilment of this requirement guarantees that total internal reflection can occur. A light source will irradiate to one surface of the prism and in the direction of the boundary between the prism and the external medium. In the case of the developed sensor, the light

Table 1. State of art of the most common commercial and academic sensing mechanisms.

Commercial prism-based sensors			
	Range (RIU)	Resolution (RIU)	Ref.
Abbe refractometer	1.3–1.7	10^{-4}	[2]
Lab. digital refractometer	1.3–1.6	10^{-5}–10^{-4}	[3]
Intrinsic intensity based sensors			
	Range (RIU)	Resolution (RIU)	Ref.
Macrobending (POF)	1.3–1.59	5×10^{-3}	[4]
D-shape (POF)	1.33–1.44	6.48×10^{-3}	[5]
Taper	1.37–1.40	5×10^{-4}	[6]
U-shaped clad removed taper (POF)	1.33–1.45	5×10^{-4}	[7]
Twisted tapered (POF)	1.37–1.41	2.6×10^{-4}	[8]
Gratings and grating-based interferometric sensors			
	Range (RIU)	Resolution (RIU)	Ref.
Etched FBG Fabry–Pérot	1.33–1.4	1.4×10^{-5}[a]	[9]
LPFG Fabry–Pérot taper	1.333–1.362	5.8×10^{-6}[a]	[10]
TFBG	1.415–1.455	3×10^{-5}[a]	[11]
Non-grating interferometric based sensors			
	Range (RIU)	Resolution (RIU)	Ref.
Fabry–Pérot PCF based	1.33–1.45	1.2×10^{-5}	[12]
Sagnac loop PCF	≈1.333	4×10^{-6}[a]	[13]
P–D fibre Sagnac loop	1.33–1.36	2.46×10^{-4}[a]	[14]
Taper Michelson interferometer	1.33–1.36	5.1×10^{-4}[a]	[15]
Core offset Mach–Zehnder	1–1.0022	6.2×10^{-6}[a]	[16]
Microfluidic PCF sensor	1.40–1.44	1.2×10^{-7}[a]	[17]
SPR based sensing			
	Range (RIU)	Resolution (RIU)	Ref.
Wavelength interrogation prism	—	10^{-6}[a]	[18]
Uncladded fibre silver film	1.33–1.39	1.5×10^{-6}[b]	[19]
Uncladded fibre gold nanoparticles	1.33–1.41	2×10^{-5}[b]	[20]
Fibre D-shaped gold film	1.33–1.39	6.3×10^{-6}[b]	[21]
Fibre taper gold film	1.435–1.445	4×10^{-7}[b]	[22]
TFBG gold film	1.33–1.38	1×10^{-5}[b]	[23]

[a] 1 pm spectral analyser resolution.
[b] 10 pm spectral analyser resolution.

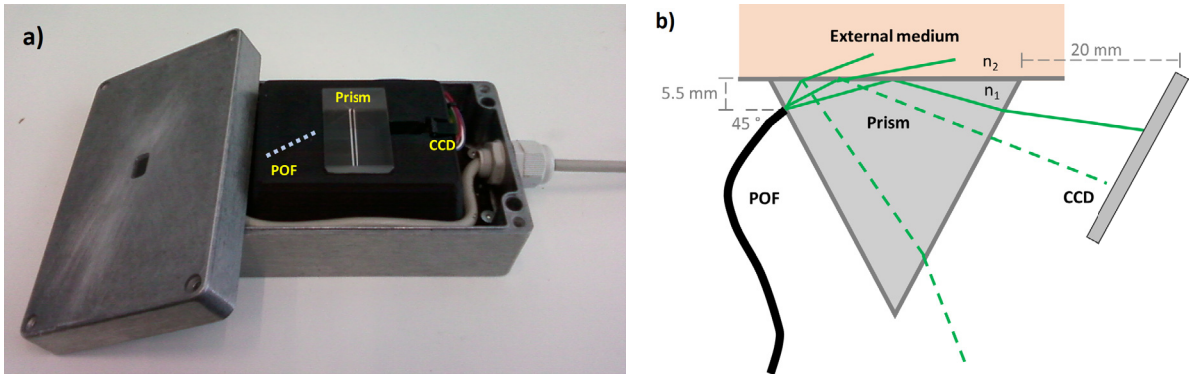

Figure 1. (a) RI sensor with the components cased in an aluminium waterproof box; only the prism is in contact with the external medium. (b) Scheme of the sensor's physical principle when the liquid of the external medium is in contact with the prism.

will come from a plastic optical fibre (POF, GHCP4001 from Mitsubishi) having an ideal numeric aperture (NA) of 0.5, which will not spread the light in a wider cone as would happen with direct usage of a LED, but will be sufficient to have a good range of light ray angles. Using a POF also prevents the need to use a set with a LED and lens to focus the light, which simplifies the sensing system in comparison with a traditional refractometer. When light reaches the interface with an incident angle θ_i below the critical angle of total reflection, that is, when $\theta_t = 90°$, it is partly transmitted into the liquid, whereas for higher angles the light is totally reflected, creating a dark region and a lit region on the other face of the prism. The angles at which the light will be reflected or transmitted will be totally dependent on the liquid RI value. At some distance from the prism, a CCD sensor (model TCD1304DG, from Toshiba Electronic) with a 8 μm pixel resolution is placed to detect the lit/dark boundary regions. Depending on the detected position of this boundary, the RI of the liquid can be assessed. Since the only measured parameter is the position of the boundary, the light intensity is irrelevant as long as it is high enough to be detected and does not saturate the CCD sensor. The LED light source used was a 522 nm model (IF E93, from Industrial Fibre Optics). Both the LED source and CCD sensor array were controlled by a Raspberry Pi 3 with wireless capability.

To accommodate the components at the desired distances and angles presented in figure 1(b)), a solid structure is required. This structure was made by 3D printing and is placed in a waterproof box with a rectangular-cut section in the top to place and assure the contact of the prism with the external medium (figure 1(a)). The 45° angle and the 5.5 mm distance chosen for the fibre are optimized so that the prism surface is guaranteed to be in contact with the liquid and is illuminated so that the light reaches this interface with the right angles necessary to observe the lit/dark boundary region in an acceptable RI range.

A temperature probe sensor (DS18B20, from Maxim Integrated) is also present inside the measurement box, in direct contact with the prism, since the measurements will be dependent on the prism temperature and a compensation needs to be carried out after calibration. The electrical connections to the CCD, LED and the temperature probe are made possible through a lateral-cut section of the measurement box, properly sealed, from which an electrical cable passes and assures the electrical power requirements.

2. Experimental results

The sensor can be remotely activated to proceed for a measurement. The procedure consists of the following steps: the sensor turns on the LED at the necessary time to obtain a profile of the light reaching the CCD; that is, the intensity is detected for each one of their effective 3650 pixels. The typical raw data profile of measurement when in a liquid can be observed in figure 2(a)); the measured signal presents some noise, but the profile of the signal is perfectly visible. It is important to note that the CCD raw measurement comes directly from the dark signal intensity. This means that the maximum values obtained will be related to a darker spot, while, when detecting light, the values will be lower. So, by analysing the typical profile, we can deduce that the first pixels are in a darker region which becomes less dark until it reaches a spot with total internal reflection. The slope observed reaches the maximum value at the boundary, where there is a transition from the dark region to the lit region. However, this value cannot be used since it is not reliable due to the signal noise. After the detected low signal (lit region) there is an increase of the signal. This increase is due to a permanent dark region. This part of the signal is not used posteriorly for the data analysis and measurement assessment. The contrast of the dark signal intensity between the dark/lit regions can be improved in two ways. The first is by increasing the integration time of the CCD to receive more light; however, this presents a complication of increasing also the signal-to-noise ratio. The second way is to use low integration times in the CCD but using a higher intensity power source.

To prevent a high quantity of data transmission the wireless communication system, instead of transmitting the information of each pixel, a simple data manipulation, i.e. a smoothing technique based on a moving average (red line in figure 2(a)), is implemented within the board processor. This solution also presents possible future improvements by using a dedicated home-made board with a low-end microcontroller.

After the smoothing process, values at key positions are gathered, which include the following: the first value of the curve, which is the maximum; the minimum value of the curve; and

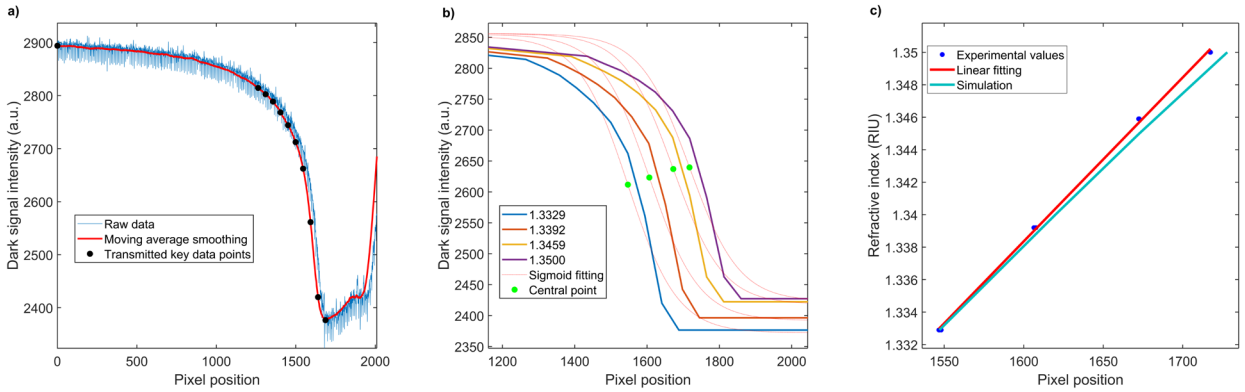

Figure 2. (a) Typical RI profile measurement in a solution obtained from the CCD. A moving average smoothing is performed to obtain key data points from the profile. (b) Evolution of the central point obtained from the fittings of the reconstructed signal with the increase of the RI. (c) Comparison of the experimental values obtained by the sensor with the increase of RI and the expected behaviour from the simulation.

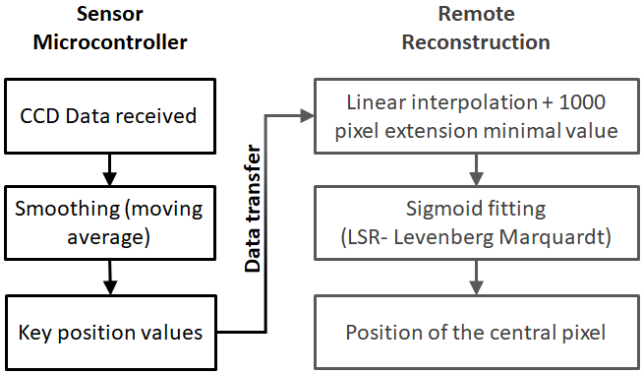

Figure 3. Diagram of the data operating principle in the sensor microcontroller and after the transference to a remote server.

Table 2. Parameters of the obtained regression of the experimental values and the simulation from figure 2(c)).

	Linear model: $y = ax + b$			
	a (RIU^{-1})	b (RIU)	R^2	RMSE
Linear fitting	1.01×10^{-4}	1.177	0.9992	1.98×10^{-4}
Simulation	0.95×10^{-4}	1.187	—	—

nine representative points of the boundary slope that are important to identify its position for an effective RI measurement (dark dots in figure 2(a)). These key points possess all the necessary information to successfully and remotely reconstruct a smoothed curve. An on-line server is an example to where these data could be sent to remotely reconstruct the curve obtained from the sensor. When this information is received, the reconstruction of the curve is done using a linear interpolation between the key values with an added extension of the minimal value for more than 1000 pixels that will emulate the lit region. These pixels will be important for the consequent sigmoid fitting applied to the reconstructed curve using a least squares regression (LSR) with a Levenberg–Marquardt algorithm. The sigmoid equation is

$$y = \frac{A_1 - A_2}{1 + e^{(x-x_0)/dx}} + A_2 \qquad (2)$$

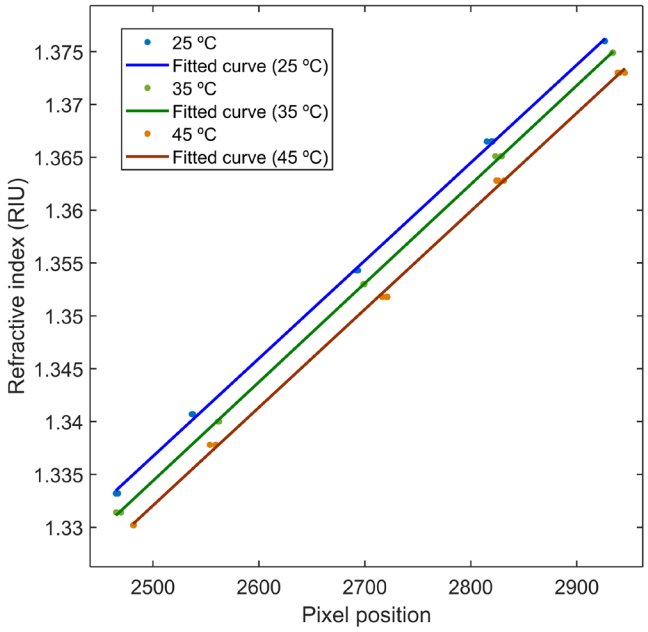

Figure 4. Pixel position increase with the RI obtained with the developed sensor when measured in clear solutions with 25, 35, and 45 °C temperature.

with A_1 and A_2 the horizontal asymptotes, where A1 is the upper value and A2 is the lower. The slope of the sigmoid is calculated by $(A_1 + A_2)/4dx$. The central point position has coordinates of $(x_0, [A1 + A2]/2)$ with x_0 being the value that will indicate the measured pixel position. This will be related to the boundary and consequently to the RI value measured (figure 3).

The RI characterization was performed using water solutions with sucrose, and the RI values were measured in a bench refractometer (Abbemat 200, from Anton Paar GmbH) with a temperature of 20 °C. For each sample, three independent measurements were performed. Figure 2(b) presents the evolution of the reconstructed signal with increases of RI in a range between 1.3329 to 1.3500 RIU. The figure also shows for each curve the related sigmoid fitting with its central point clearly identified as a green dot. The linear fitting

Table 3. Mean pixel position values and standard deviation values from the three measurements represented from figure 4.

	RI (RIU)	Pixel position mean	STD
25 °C	1.3332	2466	1.14
	1.3407	2537	0.57
	1.3543	2692	0.66
	1.3665	2818	2.81
	1.3760	2926	0.32
35 °C	1.3314	2466	2.53
	1.3400	2562	0.44
	1.3530	2699	0.58
	1.3651	2827	3.37
	1.3749	2933	0.38
45 °C	1.3302	2481	0.28
	1.3378	2557	3.16
	1.3518	2719	2.55
	1.3628	2827	3.82
	1.3730	2941	3.57

Table 4. Parameters of the obtained regressions from the temperature variation measurements from figure 4.

	Linear model: $y = ax + b$			
	a (RIU^{-1})	b (RIU)	R^2	RMSE
Linear fitting (25 °C)	0.93×10^{-4}	1.105	0.9994	4.01×10^{-4}
Linear fitting (35 °C)	0.94×10^{-4}	1.100	0.9999	2.02×10^{-4}
Linear fitting (45 °C)	0.93×10^{-4}	1.100	0.9992	4.74×10^{-4}

of the experimental results and a simulation of the expected results from this device, using all the parameters described before for the materials and geometrical measurements, is presented in figure 2(c)) and its parameters in table 2. A resolution of 1.01×10^{-4} RIU was obtained for this sensor, which is near the one expected from the simulation. A range measurement between 1.3200 to 1.3760 RIU is possible with this sensor configuration. Better resolutions could be obtained if the surface length of the prism in contact with the liquid was longer and the fibre position adjusted with a further optimization. Longer surfaces will allow a higher spread of light, which gives higher resolutions detected in the CCD, but is bulkier or requires a costly custom-made prism. Another way to increase the resolution of the sensor is to increase the distance of the prism and CCD. In both cases the range of detection is reduced.

Temperature characterization of the sensor was also performed inside a climatic chamber. The positions of the sensor head elements were slightly adjusted to guarantee a better attachment for this characterization. A temperature probe that is in contact with the prism was used for temperature measurements. A variation of the RI measurement was done with five samples between values of 1.3300–1.3760 RIU measured by the bench refractometer and for three different temperatures: 25, 35 and 45 °C (figure 4). For each sample, the measurement was repeated three times. Mean values and standard deviation (STD) calculation is presented in table 3. A linear fitting was performed for each temperature variation, and its parameters are presented in table 4. With an increase of temperature higher STD values were obtained, which shows that the system became more unstable. With a STD value of 3.82 in the

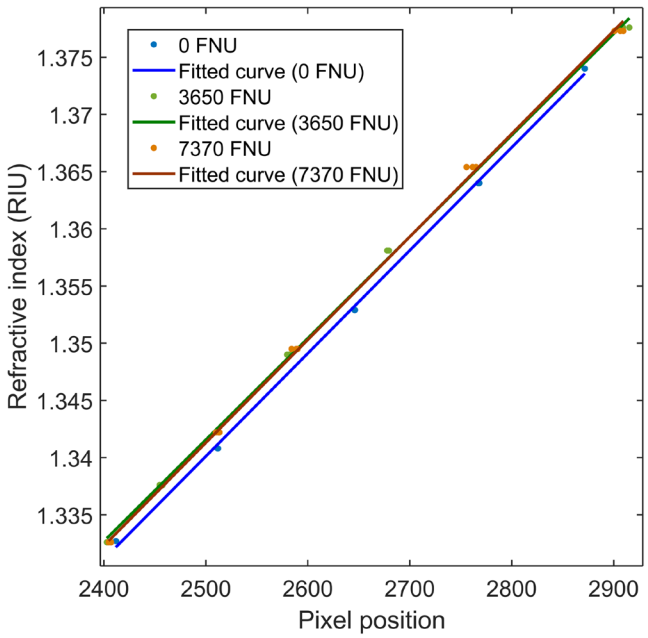

Figure 5. Pixel position variation with the RI obtained in turbid solutions with 3650 and 7370 FNU.

pixel position, an uncertainty of 3.5×10^{-4} RIU is obtained. To increase accuracy, the system will need to obtain mean values of more measurement acquisitions. An offset to the calibration line was observed with each increment of temperature. For future measurements with temperature compensation, one should obtain the pixel position and measure the temperature, then apply the necessary offset to the first calibration line (performed with constant temperature) before calculating the

Table 5. Parameters of the obtained regressions from the turbid solutions measurements from figure 5.

	Linear model: $y = ax + b$			
	a (RIU^{-1})	b (RIU)	R^2	RMSE
Linear fitting (0 FNU)	0.92×10^{-4}	1.115	0.9993	4.22×10^{-4}
Linear fitting (3650 FNU)	0.93×10^{-4}	1.120	0.9993	4.61×10^{-4}
Linear fitting (7370 FNU)	0.93×10^{-4}	1.116	0.9991	5.13×10^{-4}

RI. Note that with the adjustment in the sensor elements the obtained resolution was lower than 10^{-04} RIU.

Measurements under a turbid solution were also assessed. Water solutions containing corn starch particles were prepared with turbidity values of 3650 and 7370 formazine nephelometric units (FNU). For each turbidity value solution, sucrose was added and measured three times with the sensor. For comparison, a clear solution (0 FNU) was also measured in the same conditions. The results are presented in figure 5 and table 5. It is shown that light not totally internally reflected in the prism is scattered by the particles of the turbid liquid and is redirected to the CCD. This light will change slightly the profile of the detection signature since the CCD will receive scattered light in both the lit and dark regions. This change is enough to create a shift of 15 pixels from what is expected using clear liquids. However, this variation of 15 pixels is constant with the increase of RI, i.e. the rate of increase is the same. A turbidity compensation needs to be applied for measurements where turbidity is present to maintain the 10^{-4} resolution or a value of 1.5×10^{-3} is assumed.

3. Conclusions

The developed sensor here presented has accomplished the objectives initially proposed: in-line and real-time capability for liquids RI monitoring, low complexity of assembly and using low-cost components (as reference, the total cost for the sensor in terms of components was lower than 150 €). The obtained resolution with a magnitude of 10^{-4} RIU is comparable to most commercial beach refractometers. A temperature measurement with a temperature probe in contact with the prism can be used to compensate automatically the temperature dependence of the sensor that shifts the location of the dark/lit boundary. This sensor has the potential to be used for real-time monitoring in industrial applications such as the drinks and beverages industry, oil-based solutions industry, glycol solutions, etc. Further work will be undertaken by installing this sensor in real conditions applied to one of the described potential applications.

Acknowledgments

This work was funded by FCT/MEC through national funds and when applicable co-funded by FEDER—PT2020 partnership agreement under the projects UID/EEA/50008/2013, sWAT (P01262) and INITIATE-IF/FCT-IF/01664/2014/CP1257/CT0002. Daniel P Duarte wishes to acknowledge financial support from FCT through research Grant No. SFRH/BD/130966/2017.

ORCID iDs

Daniel P Duarte https://orcid.org/0000-0002-5845-9354
Rogério N Nogueira https://orcid.org/0000-0002-4156-8984
Lúcia B Bilro https://orcid.org/0000-0001-8804-593X

References

[1] Meeten G H 2014 Refractive index measurement *Measurement, Instrumentation, and Sensors Handbook, Second Edition: Electromagnetic, Optical, Radiation, Chemical, and Biomedical Measurement* 2nd edn ed J G Webster and H Eren (Boca Raton, FL: CRC Press) p 50
[2] Tarrant A W S 2010 Optical measurements *Instrumentation Reference Book* 4th edn, ed W Boyes (New York: Elsevier) pp 499–519
[3] Anton Paar 2018 Abbemat refractometer series: The universal refractometer 1-7 www.anton-paar.com/?eID=documentsDownload&document=60387&L=0 (Accessed: 10 November 2019)
[4] Zubia J, Garitaonaindía G and Arrúe J 2000 Passive device based on plastic optical fibres to determine the indices of refraction of liquids *Appl. Opt.* **39** 941
[5] Sequeira F *et al* 2016 Refractive index sensing with D-shaped plastic optical fibres for chemical and biochemical applications *Sensors* **16** 2119
[6] Polynkin P, Polynkin A, Peyghambarian N and Mansuripur M 2005 Evanescent field-based optical fibre sensing device for measuring the refractive index of liquids in microfluidic channels *Opt. Lett.* **30** 1273
[7] Teng C, Jing N, Yu F and Zheng J 2016 Investigation of a macro-bending tapered plastic optical fibre for refractive index sensing *IEEE Sens. J.* **16** 7521–5
[8] Teng C *et al* 2019 Refractive index sensor based on twisted tapered plastic optical fibres *Photonics* **6** 40
[9] Liang W, Huang Y, Xu Y, Lee R K and Yariv A 2005 Highly sensitive fibre Bragg grating refractive index sensors *Appl. Phys. Lett.* **86** 151122
[10] Ding J-F, Zhang A P, Shao L-Y, Yan J-H and He S 2005 Fibre-taper seeded long-period grating pair as a highly sensitive refractive-index sensor *IEEE Photonics Technol. Lett.* **17** 1247–9
[11] Alberto N J, Marques C A, Pinto J L and Nogueira R N 2010 Simultaneous strain and refractive index sensor based on a TFBG *Proc. European Workshop on Optical Fibre Sensors* vol 7653 p 765324
[12] Wang T and Wang M 2012 Fabry Pérot fibre sensor for simultaneous measurement of refractive index and temperature based on an in-fibre ellipsoidal cavity *IEEE Photonics Technol. Lett.* **24** 1733–6
[13] Wu C *et al* 2014 In-line microfluidic integration of photonic crystal fibres as a highly sensitive refractometer *Analyst* **139** 5422–9

[14] Lu H *et al* 2018 Temperature and liquid refractive index sensor using P–D fibre structure-based Sagnac loop *Opt. Express* **26** 18920
[15] Tian Z, Yam S S and Loock H 2008 Refractive index sensor based on an abrupt taper Michelson interferometer in a single-mode fibre *Opt. Lett.* **33** 1105
[16] Duan D-W, Rao Y-J, Xu L-C, Zhu T, Wu D and Yao J 2011 In-fibre Mach–Zehnder interferometer formed by large lateral offset fusion splicing for gases refractive index measurement with high sensitivity *Sens. Actuators* B **160** 1198–202
[17] Ayyanar N, Thavasi Raja G, Sharma M and Sriram Kumar D 2018 Photonic crystal fibre-based refractive index sensor for early detection of cancer *IEEE Sens. J.* **18** 7093–9
[18] Homola J, Yee S S and Gauglitz G 1999 Surface plasmon resonance sensors: review *Sens. Actuators* B **54** 3–15
[19] Jorgenson R C and Yee S S 1993 A fibre-optic chemical sensor based on surface plasmon resonance *Sens. Actuators* B **12** 213–20
[20] Shao Y, Xu S, Zheng X, Wang Y and Xu W 2010 Optical fibre LSPR biosensor prepared by gold nanoparticle assembly on polyelectrolyte multilayer *Sensors* **10** 3585–96
[21] Lin Y-C 2013 Characteristics of optical fibre refractive index sensor based on surface plasmon resonance *Microw. Opt. Technol. Lett.* **55** 574–6
[22] Monzón-Hernández D, Villatoro J, Talavera D and Luna-Moreno D 2004 Optical-fibre surface-plasmon resonance sensor with multiple resonance peaks *Appl. Opt.* **43** 1216
[23] Caucheteur C, Shevchenko Y, Shao L-Y, Wuilpart M and Albert J 2011 High resolution interrogation of tilted fibre grating SPR sensors from polarization properties measurement *Opt. Express* **19** 1656–64